AIVP
ADVANCES IN IMAGE AND VIDEO PROCESSING

Table of Contents

Processing the Images of Dispersive Structures by Irregular Pyramid

On Supervised Methods for Segmentation of Blood Vessels in Ocular Fundus Images

A Imaging Supper-Resolution Processing Method for Effective Aperture Check of Thick Pinhole

Xie Hongwei Zhang Jianhua Zhang Faqiang Li Linbo Qi Jianmin
*Institute of Nuclear Physics and Chemistry, China Academy of Engineering Physics,
Mianyang, Sichuan, P.R. China, 621900*

ABSTRACT

The Lucy-Richardson super resolution image processing technique, combined with the introduced virtual point spread function (PSF), was used to develop a measurement method of the processing precision of the superfine thick pinhole aperture. The principles of the technique were based on the known ideal image and degraded image. After the restoration and reconstruction of the degraded image with the introduced virtual point spread function (PSF)，the comparison is made between the reconstructed image and the ideal image to judge the correctness of the virtual point spread function (PSF). During this process, the simulation of the effects of the point spread function (PSF) upon the image reconstruction was carried out at first. As indicated by the simulation, the ideal point spread function (PSF) used in the image restoration and reconstruction could provide ideal results of the image reconstruction. However, in the case of relatively bigger size of the point spread function (PSF), the reconstructed image would be obtained smaller than the ideal image. Besides, related experiments were carried out on the cobalt radiation sources. In the experiments, the aperture of the shielded collimator to restrict and align the radiation source was known to be 1.0mm, the thick pinholes respectively 0.7mm and 0.45mm in aperture were used for the imaging of the Φ1mm radiation source, and the radiation image was recorded in imaging plates 0.05mm×0.05mm in spatial resolution. Based on the hypothesis that the processing precision of the thick pinhole fulfill the experiment requirements, the point spread function obtained from the simulated computation was introduced into the restoration and reconstruction of the recorded images. At the area with an intensity of 50%, the thick pinhole with 0.7mm aperture could provide homogenous image of the radiation source. However, the thick pinhole with 0.45mm aperture provided an elliptical image with a major-minor axis ratio of 5:3. The relatively big difference between the measurement results with the actual known object size indicates the relatively big gap between the virtual point spread function with the actual or real point spread function. This could be considered to be another indirect evidence of the relatively big difference between the actual processing precision of the 0.45mm aperture with the designed requirements.

Keywords: image super resolution, thick pinhole, Lucy-Richardson, neutron imaging

1. INTRODUCTION

During the inertial confinement fusion (ICF) experiments, the reacting conditions in the fusion thermal nucleus could be obtained from the diagnostics of information of high energy neutrons, γ-rays and other particles induced by the nuclear reaction in the D-T capsule. This attempt was succeeded in the laser-driven fusion [1]. At the same time, various diagnostic methods were well developed. As one of the major diagnostic methods, the pinhole photography was used to track

and record the spatial radiation flux of the high energy thermonuclear neutrons. This technique was considered to be a preferential option in terms of various aspects. Firstly, the flux could convey such important information of the implosion process more directly including the spatial scale, shape and homogeneity. Secondly, the spatial intensity distribution of neutrons with various energy levels could further reflect the temperature distribution in the target capsule. Thirdly, the spatial intensity distribution of the neutrons is independent on the surface density of the target capsule. Based on the above considerations, in the experiments, such diagnostic methods including the pinhole neutron imaging and penumbral imaging were developed to successfully obtain the profile images of the reacting area[2, 3].

Due to the fact that the size of the imaging aperture used in the penumbral imaging is a little bit bigger than that of the radiation source, the size of the radiation source could not be obtained directly. And the image information of the radiation source could only available after image processing. As for the case of the pinhole imaging, where the size of the imaging aperture is smaller than that of the radiation source, it could provide directly the size of the radiation source. However, due to the dependence of the spatial resolution largely upon the pinhole aperture, the relatively smaller size of the pinhole aperture could provide a fairly better spatial resolution but lacks in smaller neutron flux. Thus, as a common compromise, the requirement of the spatial resolution is lowered for the purpose of an acceptable sensitivity of the imaging recording system, as well as an acceptable impact of the detecting efficiency upon the image quality. The aperture of the thick imaging pinhole used in our ICF experiments were about 30μm[3], whose spatial resolution, in dealing with the radiation sources about 100μm in size, could not fulfill the experimental requirements. Thus, the super resolution image process of the existing neutron images was considered reasonably to be an important measure to obtain better image quality.

As a major parameter in the image reconstruction, the point spread function (PSF) is dependent on both the thick pinhole aperture and the material composition of the aperture. Besides, due to the relatively strong penetration effects of the neutrons, the PSF itself is dependent upon not only the size of the straight-throng area of the pinhole, but also upon the decaying maters in the pinhole materials. The shapes of the thick pinhole are majorly in circle, or triangle and square sometimes. Another major factor to affect the PSF size is the processing precision of the thick pinhole. Generally, the thick pinhole is made of such high density maters as tungsten (W), with a thickness of over 20cm, or even more than 50cm in the extreme conditions. As for the manufacturing procedure, the thick pinhole is assembled with segmented parts. Technically, it's very difficult to obtain experimentally the effective aperture of the superfine thick pinhole due to its relatively big total size.

In dealing with this issue, several options are available. The first option is to use laser diffraction method, where the processing precision could be provided based on the analysis of the configurations of the diffraction rings. This method could provide information mainly related with the shape of the aperture in the diffraction plane. Another option to detect the thick pinhole is CT

scanning with high energy γ-rays, which, however, could not provide satisfactory detecting precision for the experiment. In our past image reconstruction process of the super resolution of the neutron images, we used the simulated computational parameters based on an ideal thick pinhole[4]. Thus, in this paper, the super resolution image processing technique, combined with the introduction of the virtual point spread function (PSF), was used to develop a new measurement method of the processing precision of the superfine thick pinhole aperture.

2. PRINCIPLES OF THE DETECTION

2.1 Basic Principles of Thick Pinhole Imaging

Generally, the image of the radiation source is imaged and transmitted onto the image plane through the thick pinhole. And the intensity of the image plane could be given in the following equation:

$$g(x, y) = \iint h(x, y, x', y', f(x', y')) \cdot f(x', y') dx' dy' \tag{1}$$

where: (x',y') is a point in the object plane, (x,y) is a point in the image plane, f(x',y') is the luminescence intensity at Point (x',y'), and h(x,y,x',y',f(x',y')) is the corresponding intensity distribution of f(x',y') at Point (x,y) according to the imaging system characteristics. Suppose the image plane intensity is in the mode of the linear superposition, and based on its theory, the image plane intensity could be given as follows:

$$g(x, y) = \iint h(x, y, x', y') f(x', y') \cdot dx' dy' \tag{2}$$

where: h(x,y,x',y') is the response function at Point (x,y) in the image plane of Point (x',y') in the object plane. Again, suppose the response of f(x',y') to h is linear. The reason to make some hypothesis is to simplify the issues. Thus, based on the supposed ideal thick pinhole imaging process, and static object plane and image plane, the above equation could be alternatively expressed as follows:

$$g = h * f \tag{3}$$

However, the effects of the noise upon the system could never be excluded in the radiography. Consequently, the image plane intensity could be given in the following:

$$g = h * f + n \tag{4}$$

where: n is the noise of the recording system.

2.2 Rucy-Richardson Super Resolution Image Processing Method

R-L is actually a super resolution imaging processing method based Bayesin's theory, which could be expressed in the following[5,6]:

$$\hat{f}_{k+1}(x,y) = \hat{f}_{k}(x,y) \left[h(x,y) * \frac{g(x,y)}{\left| \hat{f}_{k}(x,y)h(x,y) \right|} \right] \tag{5}$$

where: $\hat{f}$ is the reconstructed image obtained after repeated commutation for k times. In the case of the experiment, based on the available h (the PSF of the system) and g (the recorded image), the reconstructed image could be obtained from iteration algorithm. And the reconstructed image is largely dependent on the PSF intensity distribution.

Things are quite different in the actual application, where, the PSF is unknown or even if known but with big uncertainty to result in a certain uncertainty for the image reconstruction. Fortunately, the effects of the PSF upon the super resolution image reconstruction could be analyzed by simulated computation. Firstly, the PSF in Gaussian distribution could be used to degrade the grid image. Then super resolution image reconstruction could be carried out according to Equation (5). The reconstruction results are given in Figure 1, where the image was reconstructed with ideal PSF, PSF with 2 pixels plus in size and PSF with 2 pixels minus in size, respectively. As indicated in this figure, with a relatively smaller PSF size, the reconstruction size is larger than the original size, while with relatively larger PSF size, the reconstruction size is smaller than the original size.

reconstructed with ideal PSF   reconstructed with PSF with 2 pixels plus in size   reconstructed with PSF with 2 pixels minus in size
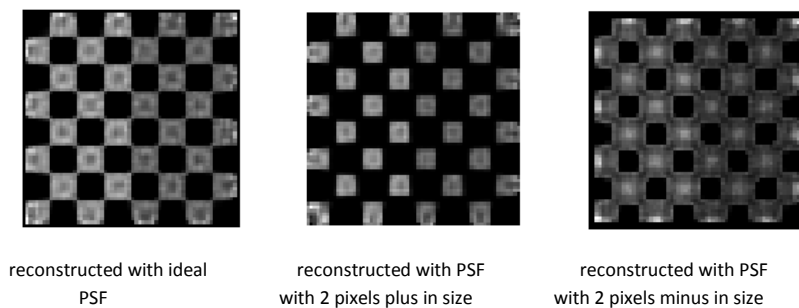
Figure 1 : The R-L reconstruction results with different PSF sizes

The super resolution image reconstruction was made mainly based on the PSF of the image diagnostic system that was mainly obtained from such methods as precision measurement. In dealing with the case, where the original image is known, but the PSF uncertainty is relatively large or even with an unknown PSF, the following equation could be used for computation:

$$\hat{h}_{k+1}(x,y) = \hat{h}_{k}(x,y) \left[f(x,y) * \frac{g(x,y)}{\left| \hat{h}_{k}(x,y)f(x,y) \right|} \right] \tag{6}$$

As indicated by Equation (3), it could be roughly concluded that Equation (5) and Equation (6) are almost same but different in expression. Thus, after the shape of the original object and the degraded image produced by thick pinhole imaging are available or known, Equation (6) could be

used for the PSF computation of the thick pinhole imaging system. The same experimental results could also be obtained with Wiener super resolution image processing method. And the test results are basically same with those obtained from such traditional measurement methods such as the slit method and edge method.

3. EVALUAION METHODOLOGY

3.1   Experimental Setup

The experiment was made with 60Co radiation source with an intensity of 8.5×103Ci and a diameter of 30mm. A collimator with an aperture of about 1mm was placed 87.1cm away from the radiation source to provide shielding and beam restriction. The imaging thick pinhole was installed 114cm away from the collimating aperture.   The image was recorded with the imaging plate, which was 197cm away from the thick pinhole. The amplification factor of the imaging system was 1.728, and the spatial resolution of the imaging plate was set to be 0.050mm/pixel.

3.2   Sensitivity Response of Imaging Plate

The imaging plate used in the experiment was provided by Fujifilm Medical Co. FCR PROFECT CS. The fluorescent reagent deliberately integrated in the imaging plate would be excited by the irradiation up to metastable state for the storage of the radiation energy. Such metastability, subject to a specific laser scanning, would be deexcited back to stable state same as that before irritation and transmit photons at the same time. The photon signals transmitted from all of pixels during deexcitation would be amplified with photomultiplier and converted in to digital signal output. Then the relationship between the image intensity and injected radiation flux could be determined by the data processing. As indicated by the experimental results, the dynamic rang of the imaging plate could be as large as up to 4 orders of magnitude. And the exposure time was appropriately determined in accordance with the relationships among the dynamic range, irradiation dosage and image intensity. In our experiment, the exposure time was set to be 1000s to provide a satisfactory signal-to-noise ratio (SNR) for the imaging system.

3.3   PSF of Thick Pinhole Imaging System

The PSF of the thick pinhole imaging system changes continuously with the change of the space. Generally, the PSF along the pinhole axis is used to interpret the spatial resolution of the thick pinhole imaging system[7]. The PSF of the thick pinhole imaging system could be obtained from the simulated computation. In dealing with a given thick pinhole, 6.5mm in material free path, 600mm in total length, 0.4mm in aperture, and 200mm in both object distance and image distance, the simulated computations of the PSF were carried out with various straight hole sections (30mm, 20mmand 10mm, respectively) and half angles of the conic strengthening segments at both ends (0.65°, 0.9° and 1.5°, respectively). The computational results are given in Figure 2. The PSF is consisting with transmittance component (the straight hole section) and the attenuation component through the pinhole matrix. And the attenuation component could be expressed by exp(-μL), where, μ is linear attenuation coefficient and L is the pass-throng thickness of γ-rays in the

attenuation matters. The amplification factor is the function of the PSF size, whose PSF could be given as r=D(1+M). In this equation, D is the pinhole diameter and M is the amplification factor.
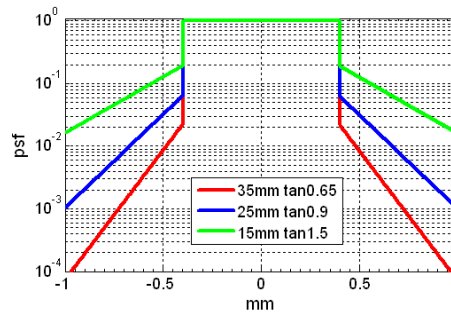

Figure 2: The structural diagram of the thick pinhole PSF

4. EXPERIMENTAL RESULT

During the experiment, a shielding collimator 1mm in aperture was used to provide beam restriction for the radiation source 30mm in diameter, as well as an equivalent radiation source Φ1mm in area. Then thick pinholes, 0.7mm and 0.45mm in aperture were used for imaging. With the laser beam as the benchmark, the collimator was aligned to be coaxial with the thick pinholes. The PSF along the pinhole axis is given in Figure 2. As for the thick pinhole with a straight hole section of 20mm, the effective clear aperture at 1% intensity attenuation would be expanded by about 0.1mm equaling to 2 pixel value. In this sense, the PSF of the ideal thick pinhole was used for the super resolution image reconstruction during the data processing.

The original image and reconstructed image obtained with 0.7m thick pinhole are given in Figure 3. As indicated in the figure, the reconstructed image is basically in circular, and the size at the 50% intensity is about 1mm. The original image and reconstructed image obtained with 0.45m thick pinhole are given in Figure 4. The reconstructed image is elliptical with a major-minor axis ratio of 5:3. Along the minor axis direction, the corresponding size at 50% intensity is about 1mm, indicating that this direction is corresponding to the 0.45mm pinhole thickness while the major axis direction is corresponding to the 0.7mm pinhole thickness.
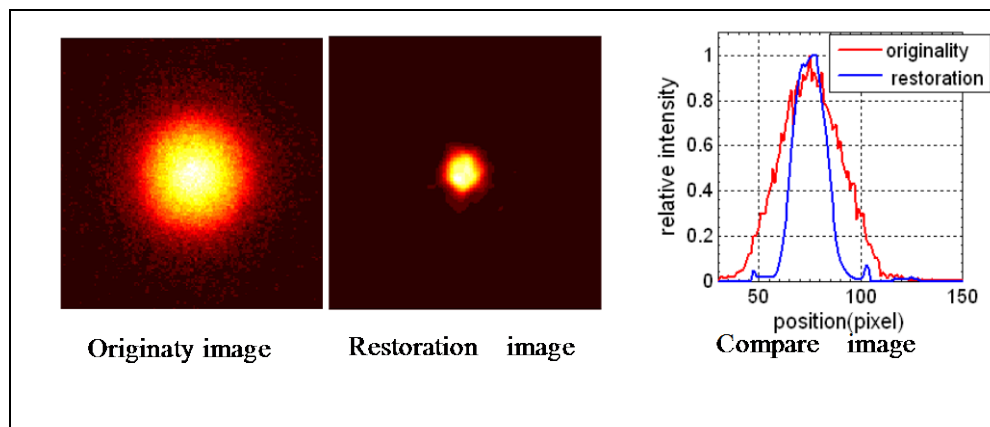

Figure 3 : The original image and reconstructed image obtained with 0.7m thick pinhole
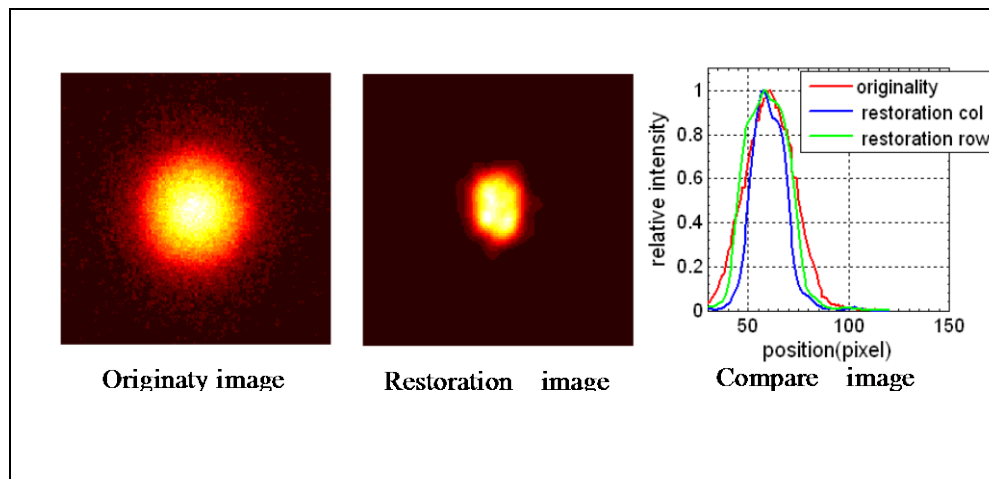
Figure 4 : The original image and reconstructed image obtained with 0.45m thick pinhole

5. DISCUSSION

5.1   Processing Precision of 1mm Thick Pinhole

During the processing of the superfine thick pinhole, the electrical discharge machining method was used to prepare a small pinhole aperture in about 0.2-0.3mm. Then, the low-speed wire grinding process on precise machine would be carried out to finish the fabrication of the thick pinhole. The precision of the product is dependent on the precision of the machine. Based on the confidence of the existing science and technology, the precision could presumably well fulfill the experimental requirements. During the experiment, the PSF of the 0.7mm thick pinhole was used for the super resolution image reconstruction. The size at 50% intensity was obtained to about 1.0mm and basically in circular shape. This could be considered as a roughly accordance of the hypothetical PSF of the thick pinhole with the ideal PSF, which provide an additional indirect evidence for the processing precision of the 0.7mm thick pinhole.

5.2   Processing Precision of 0.45mm Thick Pinhole

The super resolution image reconstruction was made for the images obtained with 0.45mm thick pinhole. The perpendicular/horizontal size ratio was about 5:3 at 50% intensity. The measurement results obtained with 1mm thick pinhole was quite different from those with 0.7mm thick pinhole. In terms of the fact that there's one but only one real image, the processing precision of the 0.45mm thick pinhole would be concluded unacceptable for the design requirement.

5.3   Evaluation of Measurement Precision

Since the PSF of the thick pinhole imaging system is determined by D(1+1/M), the PSF should be a major cause for the image degradation. In the ideal conditions, after the super resolution image reconstruction, the maximum correction size would roughly equal to the PSF size. In addition, the minimum precision of the image restoration is determined by the spatial resolution of the image

recording system.   Thus, the ultimate precision in our experimental measurement could be determined to be about   0.05mm.

5.4   Reasons for Why not to Apply This Method into PSF Computation of Thick Pinhole Imaging System Directly

In our experiment setup, a 1.0mm collimating aperture was indeed placed in front of the radiation source. However, the collimating aperture was 87.1cm away from the radiation source and 114cm away from the imaging aperture at the same time. In accordance with the pinhole imaging principles, the collimating aperture would be considered as a penumbral intensity distribution. Hypothetically, the ideal intensity of the object plane should be a homogenous transmittance. Actually, with this additional 1mm radiation collimator, the distribution in a 1mm area in the aperture could not be homogenous. Thus, the PSF could not be determined with Equation (6), because this equation is only available for the ideal image and recorded image with homogenous intensity.

5.5   Spatial Resolution of Imaging Plate

In the experiment, the imaging plate was used to record the radiation image, but the effects of the imaging plate on the image processing were excluded from the super resolution image reconstruction.

6. CONCLUSION

The major application of the superfine thick pinhole was dealing with the image diagnostics of the high energy neutrons and γ-rays. The super resolution image processing, combined with the virtual PSF, was used to develop a new measurement method for the precision of the thick pinhole aperture. This method is based on the known image of the original object. And the correctness of the virtual PSF would be determined based on the comparison of the reconstructed image and the original image.

In this paper, the simulated study was presented. After that, imaging process was made for a radiation source 1mm in effective size with thick pinholes respectively 0.7mm and 0.45mm in aperture (a 1mm aperture collimator was used to provide beam restriction for the radiation source). Then, the super resolution image reconstruction, combined with the virtual PSF, was used to measure the processing precision of the thick pinhole. As indicated theoretically and experimentally, this method is concluded to applicable, reliable and simplified, which could provide the effective PSF of the thick pinhole imaging system.

REFERENCES

[1]. Ress D,Lerche R A, Eill R J, Neutron imaging of laser-fusion targets,Science,Vol.241,p956-958,1988.

[2]. Sommargren G E,Lerche R A, Neutron Imaging of ICF Target Plasmas, review of scientific instruments, Vol.74, No.3, p1832-1836, 2003.

[3]. C. R. Christensen, Cris W. Barnes, First results of pinhole neutron imaging for inertial confinement fusion, review of scientific instruments, Vol. 74, No.5 , p2690-2694, 2003.

[4]. S. D. Metzler, J. E. Bowsher, Analytic Determination of the Pinhole Collimator' Point-Spread Function and RMS Resolution With Penetration，IEEE TRANS ON MED IMAG VOL. 21, NO. 8, p878-887, 2002.

[5]. Sungchae Jeona, Gyuseong Choa,ea tl'Determination of point spread function for a flat-panel X-ray imager', Nuclear Instruments and Methods in Physics Research A 563,167-171, 2006.

[6]. David A. Reimann, Hooly A. Jacobs, Use of wiener filtering in the measurement of the two dimensional modulation transfer function, SPIE Vol.3977，P670-680，2000.

[7]. Xie Hong wei, Thick pinhole design applied to high energy ϒ ray source radiographic diagnostics, Nuclear Electronics & Detection Technology, Vol.31 No.2, P143-147, 2011.

Processing the Images of Dispersive Structures by Irregular Pyramid

Tatiana Ruzova[1], Vladimir Yeliseyev, Alexander Tolstopyat, Leonid Fleer
Faculty of mechanics and mathematics, O. Gonchar Dnepropetrovsk National University,
Dnepropetrovsk, Ukraine 49010, prosp. Gagarina, 72, Dnepropetrovsk, Ukraine;
[1]E-mail: *ruzov1973@bk.ru*, +38-098-243-06-55

ABSTRACT

The paper deals with the improvement of irregular pyramid method for processing images of dispersed formations and other microscopic objects. The method is based on the natural aggregation of adjacent image areas from one pyramid level to another and can process noisy images of different sized objects with non-uniform brightness. The developed method combines image segmentation, filtration and binarization operations.

There is made analysis of topological problems caused by applying the different types of pixels connectivity. Algorithms determining the adjacent image areas and internal hollows in connected pixel sets are designed on the basis of analysis. Proposed algorithms may be applied to local image segmentation. Using algorithms for constructing different hierarchical levels of Meer pyramid and dispersed formations images segmentation will provide more precise objects structure and avoid over-detailing. There is proposed method for sliding window size evaluation for local segmentation methods applied to processing dispersion environments images by irregular pyramids method.

Keywords: segmentation, filtration, video images, dispersed formations, irregular pyramid.

1. INTRODUCTION

Object segmentation is one of the main and perhaps the most difficult stages of image processing. The complexity of this problem lies in the possibility of changing the whole spectrum of image parameters in a wide range. The images may be of different brightness, background noisiness etc. Besides, these differences may occur within the same image set, and even more – in the same image. Images of real objects have inhomogeneous background; this feature also should be considered. On the other hand, there is no uniform standard of image quality. Therefore, despite the large number of image processing methods and algorithms [1-4],

the problems of images filtration, segmentation and binarization (especially for dispersed formations images), do not lose their actuality and do not have a universal solution.

Even such well-known methods as a threshold global segmentation are often inefficient due to the impossibility of determining single threshold for entire image. The method of histogram shape analyzing does not always lead to satisfactory results because of image noise, which causes multimodal histograms. Otsu method [5] is based on the calculating the statistical characteristics of the image pixels. This method also is also reduced to calculating entire image threshold, separating sets of object and background pixels in the most effective way. This method is effective in the case of image uniform illumination.

Methods of local segmentation are more flexible. They are based on evaluating threshold value for each part of the image (window), which size is predetermined [6]. However, for adaptation them to the images of other dispersed environments some reconfiguration of these methods consisting in refining threshold function coefficients and window size is required.

The purpose of investigation is to develop a method providing determination of objects varying in size and brightness, and combining image segmentation, filtration and binarization operations. This problem can be efficiently solved by using irregular pyramids structure.

2. CONSTRUCTION OF AN IRREGULAR PYRAMID FOR DISPERSED FORMATIONS IMAGES

2.1 Irregular pyramid structure

The proposed method uses the irregular pyramids structure and is based on the natural aggregation of adjacent image areas from one pyramid level to another.

Irregular pyramids method by Meer [7] is based on graph theory. Irregular pyramid is a sequence of nodes set R_0, …, R_N restricting at each level. Zero or base pyramid level R_0 is the original image. Each node of the next, decimated pyramid level corresponds to connected set of nodes of the previous level. That is

$$P_{t+1}=T(P_t), \text{ where } |R_{i+1}|<|R_i|, \quad R_{i+1} \subset R_i, \quad i=\overline{0,N}. \tag{1}$$

So, if the algorithm is applied to original image, at the output we obtain a set of nodes, each of them corresponds to the specified object in the image. Irregular pyramid structure is shown in Figure 1.
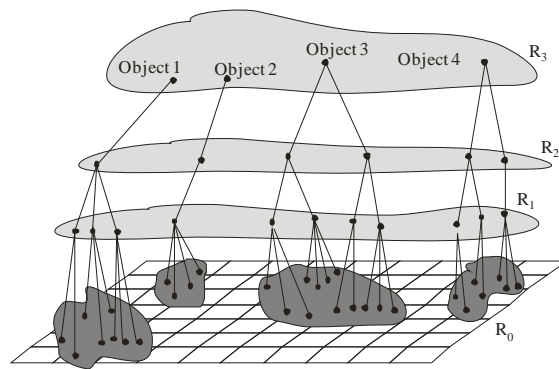
Figure 1: Irregular pyramid structure

From expression (1) it is clear that the key point in algorithm designing is the choice of the transforming function T, providing to obtain subset R_{i+1} from R_i nodes set. Function T is the criterion for moving from one pyramid level to another. It selects supporting (also mentioned as survivors) nodes among the previous level nodes for making the next level. Function T is also known as the decimation function. Child nodes of $i+1$ level are formed from the non-survivors (not included in the next $i+1$ level) nodes. This technique provides the relationship from any pyramid level down to its base.

Each stage of algorithm consists of following steps:

- Determination of the neighboring regions;

- Evaluation of T-function value ("surviving threshold") for each node of set R_i.

- Nodes of greater "surviving value" than the threshold form supporting nodes subset R_{i+1}, forming the next $i+1$ level;

- For each supporting node of set R_{i+1} it is formed connected set of children from R_i nodes neighboring to considered one. Graph nodes at i level are considered neighboring if their children are neighbors at the base level.

The process is complete, if $\left| R_{i+1} \right| = \left| R_i \right|$ there is no further thinning of pyramid levels.

Let's consider algorithm in detail.

2.2 Zero (Basic) Pyramid Level Design

The process starts from analysis of given image. Images of dispersed formations are characterized with non-uniform brightness and noisy background. Objects contours are darker in comparison with background. We propose to put in the pyramid base the pixels corresponding to figures contours after elimination of noise and background elements. To ensure method quality independence, and provide it applicability to images of other environments, filter parameters are not appointed, but evaluated based on the correlation of image parameters. Due to the fact that image brightness and noisiness may be non-uniform, it is advisable to consider each pixel in the context of its surroundings in some neighborhood.

So, the first step is supporting pixels determination. Authors propose to calculate the following global features of the image:

Global average brightness

$$Gab = \frac{\sum\limits_{\substack{x=0,W-1 \\ y=0,H-1}} g(x,y)}{W*H} , \qquad (2)$$

Horizontal contrast

$$Gac_h = \frac{\sum\limits_{x=0,W-2} |g(x+1,y)-g(x,y)|}{W*H}, \quad y=\overline{0,H-1}, \qquad (3)$$

Vertical contrast

$$Gac_v = \frac{\sum\limits_{y=0,H-2} |g(x,y+1)-g(x,y)|}{W*H}, \quad x=\overline{0,W-1}, \qquad (4)$$

Global average contrast

$$Cac = (Gac_v + Cac_h)/2 , \qquad (5)$$

where $g(x,y)$ brightness of (x,y) pixel; W, H – image width and height.

Local brightness features *Lab* and *Lac* (local average brightness and local average contrast) for each considered pixel (x, y) and its neighborhood $(x-w, y-h, x+w, y+h)$ should be evaluated in this way. The pixels with high contrast neighborhood only should be taken into consideration, because they are most likely to contain the object. Such neighborhoods (Figure 2, neighborhood A) are characterized by the relationship

$$\frac{Lac}{Gac} >= 1.05 , \qquad (6)$$

(local contrast is more than the average value). Pixel (x, y) generating such neighborhood will be inserted in supporting nodes list, if it is darker then background in this neighborhood and contrast enough, i.e.

$$Lav - g(x,y) \geq Gac \qquad (7)$$

Area B (Figure 2), containing the noise and do not containing any objects of interest, does not satisfy (7) and its pixels will not be included in the supporting nodes set. Thus, we are protected from noise influence.

In the case if the entire neighborhood belongs to object, so it is a low-contrast region (Figure 2, area C)

$$Lac < 0.2 \,, \tag{8}$$

which brightness is lower than the average brightness of the image *(g(x,y)<Gav).* Let's introduce following criterion for inclusion its pixels to the supporting points list

$$1 - \frac{g(x,y)}{Gav} > 0.05 \tag{9}$$
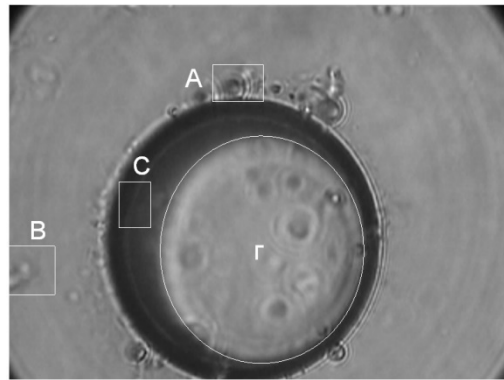
Figure 2: Neighborhoods of different types

This relationship also prevents overdetalizating the contours of objects of non-uniform brightness. Thus, expressions (6) - (9) represent an image self-adjusting filter.

The next step is child nodes selection. Let's assign some connected set of child pixels to each supporting node. For this purpose it should be done local segmentation within the smallest (3 x 3) 8-connected neighborhood of supporting pixel. Average brightness value in this neighborhood will be taken as threshold. The pixels which brightness is less than calculated threshold will be considered children. Since the considered supporting pixel is the center of such neighborhood, set connectivity is not violated for any choice of child points. Pixels forming the base level of the pyramid are shown in black in Figure 3.

Figure 3: Base level of pyramid

Pyramid base level in this interpretation is monochrome and partially filtered version of the original image. If binarization is the final goal and there is not a segmentation problem in its general formulation implying relationships between the pixels forming specified object, there is

no need in making other pyramid levels. Thus, in Figure 3 there is shown selection of entire pixel mass characterizing all objects, but these data cannot be used for analytical determination the objects number, their relative positions and geometric parameters. To determine if the pixel belongs to the particular object one should make higher pyramid levels.

2.3 Higher Pyramid Levels Design

– Determining neighboring supporting nodes for each supporting node.

– Evaluate *T*-function value for each node. This value is the number of neighboring supporting nodes.

– The threshold value of surviving function *T* is defined as an average number of neighboring nodes. Supporting nodes which surviving value is greater than threshold, assign the supporting nodes at the next level.

– Non-surviving neighboring nodes are attached to list of children. Specificity of dispersed structures segmentation consists in the fact that object is a kind of ring, i.e. has dark contour, bounding the light area (which is a part of the object too), this feature is caused by optical effects on the participles surface. Therefore, internal area nodes contained within the selected child sets should be attached as children nodes. Identification of such areas is made by algorithm described below.
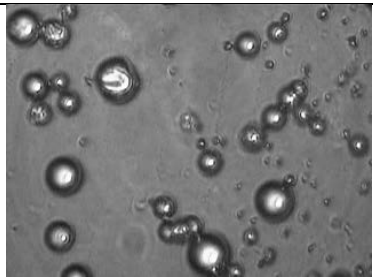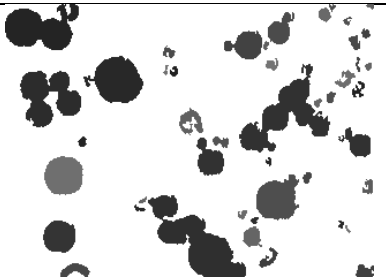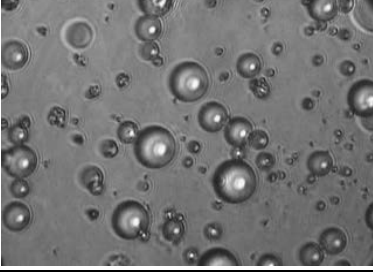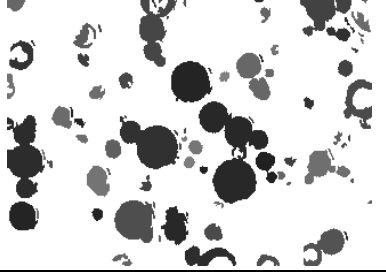
At a certain pyramid level there is a situation when the nodes number ceases to decrease due to the impossibility of further merging because of neighborhood absence, each supporting node corresponds to the entire isolated object (for clarity, unique color is assigned to each object), this fact is a criterion for algorithm termination. Figure 4 shows results of method application to the image in Figure 2.

Figure 4: The top level of the pyramid for the image in Figure 2

The results of application of this method to several images of the water-oil emulsions are shown in Table. 1.

Table 1   Segmentation of water-oil emulsion by irregular pyramids

No	The original image	Resulting image
1		
2		
3		

At the end of algorithm procession, additional filtering of selected objects based on their geometrical or morphological characters may be done. So, in our case, for images containing more or less homogeneous objects (see Table 1), it is advisable to perform filtering to eliminate the drops of low pixel weight (less than 5% of average pixel weight of all identified objects).

3. APPLYING DIFFERENT TYPE OF PIXELS CONNECTIVITY TO IMAGE PROCESSING

Concepts of 4- and 8- connected regions are often used for image recognition. But applying the both types of connectivity causes some topological problems. If the pixels forming the object are considered to be 4-connected, we get the following anomaly: the vertical and horizontal sections of the border will be connected, but the inclined ones – will not. For example, line inclined at 45° to the raster grid lines is presented not as solid object (as it is in fact), but as a set of odd pixels. This fact causes to the multiple breaks in the object contour (Figure 5(a)).

If objects boundaries are considered in terms of 8-connectivity, inclined parts are correctly identified, but background areas will be connected too, so the sloping line shown in Figure 5(b)

does not divide the field in two areas and the white pixels are connected in spite of the a black line separating them.

(a)   **(b)**
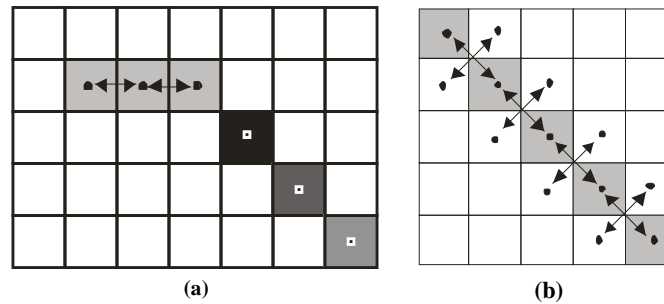
Figure 5: (a) Topological anomalies when using 4-connectivity principle; (b) Topological anomalies when using 8-connectivity principle

To solve this problem, we propose to apply different connectivity types to objects and to background. 8-connectivity is applied to object pixels, and 4-connectivity to background pixels. In this case, the object shown in Figure 6 will be a "ring", dividing the field of the image in two areas – internal and external.
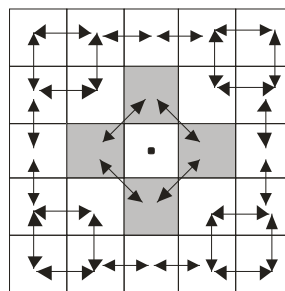
Figure 6: Application of different connectivity types to object and background pixels

In accordance with introduced connectivity criteria algorithm for areas filling [9] is improved to process not only the 4-connected (as in standard case), but the 8-connected regions. Based on this improvement, the algorithms for image segmentation are developed and applied to irregular pyramid method.

3.1 Algorithm for adjacent areas determination

To determine whether the two connected pixel sets X_1 and X_2 are adjacent, i.e. if $X_1 \cup X_2$ set is connected, the following algorithm is proposed:

- Make the convex hull for each set.

- Check if the convex hulls are overlapping. If no, X_1 and X_2 are not overlapping too.

- Otherwise paint the areas corresponding to these sets in the same color. Determine the connectivity of $X_1 \cup X_2$ set by pouring it with contrasting color using above mentioned filling algorithm, starting from some point A (Figure 7) of X_1 set. If the sets are adjacent, algorithm automatically fills X_2 area. So, if the color of any X_2 point is changed (in point B, for example) to the given color, X_1 and X_2 are adjacent.

— After merging adjacent regions joint convex hull will be made.
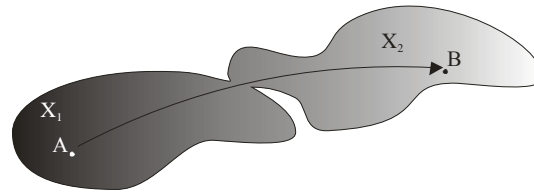
Figure 7: Scheme of $X_1 \bigcup X_2$ set connectivity definition

3.2 Algorithm for determining internal hollows in connected set

Developed filling algorithm are applied to determinating the internal hollows of connected sets. Area of interest are placed into some rectangle, height and width of it are 2 pixels larger than circumscribed rectangle (Figure 8, a). Then fill an external towards the object part of the rectangle with some contrast color considering it in terms of 4-connectivity. In this case, isolated internal hollows keeps original color (Figure 8, b). The points which have kept original color, will be attached to considered set (Figure 9, c) . This approach provides us to process not only the dark contours of drops, bubbles and other dispersed formations, but the whole "body" of participles containing glares.

a   b   c
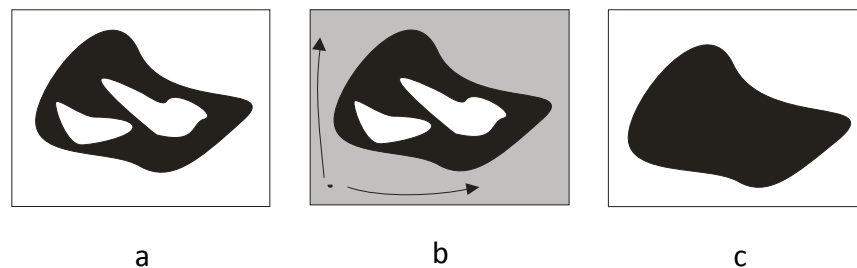
Figure 8: Scheme of internal hollows determination by using the filling algorithm

4. EVALUATE SLIDING WINDOW SIZE AT THE BASE PYRAMID LEVEL

The question of choosing sliding window size while constructing of base pyramid level is still open. Experiments on determining the influence of window size on segmentation results show that the small window size causes noise gaining, while too large one leads to brightness and contrast parameters averaging over a large area and cause small objects elimination.

Influence of sliding window size on segmentation quality of water-oil emulsions images (Table 1) is shown in the chart (Figure 10). As conventional criterion K (ordinate) is taken average brightness of supporting pixels ($\overline{g_{sup\,port.}}$) at base level divided by the average image brightness.

$$K = \frac{\overline{g_{sup\,port.}}}{Gav} \ .$$

$$(10)$$

As it is shown in the picture, applying sliding window of small area ~ 0.1 % (1p. x 1p. , 3p. x 3p.) of image area, the average brightness of supporting pixels is high, because of capturing the large mass of background elements (noises) that falls as the window area increases and reaches its minimum at a window area ~ 0.3 % - 1.3% of image size, then it increases again due to excessive brightness averaging, leading to the contours roughening and the adjacent areas capture. Thus, sliding window size for water-oil emulsions images segmentation advisable to choose within these limits. The curve corresponding to image in Figure 2, reaches its minimum at a larger window size - 2.21 % due to a significant difference between the structure of this image and other images containing number of objects. One drop in Figure 2 occupied ~ 32 % of image area.

| a | b | c |

Figure 9: Segmentation using sliding windows of different sizes: a – original image (320p. x 237p.); b – 1p. x 1p. window; c – 30p. x 30p. window;
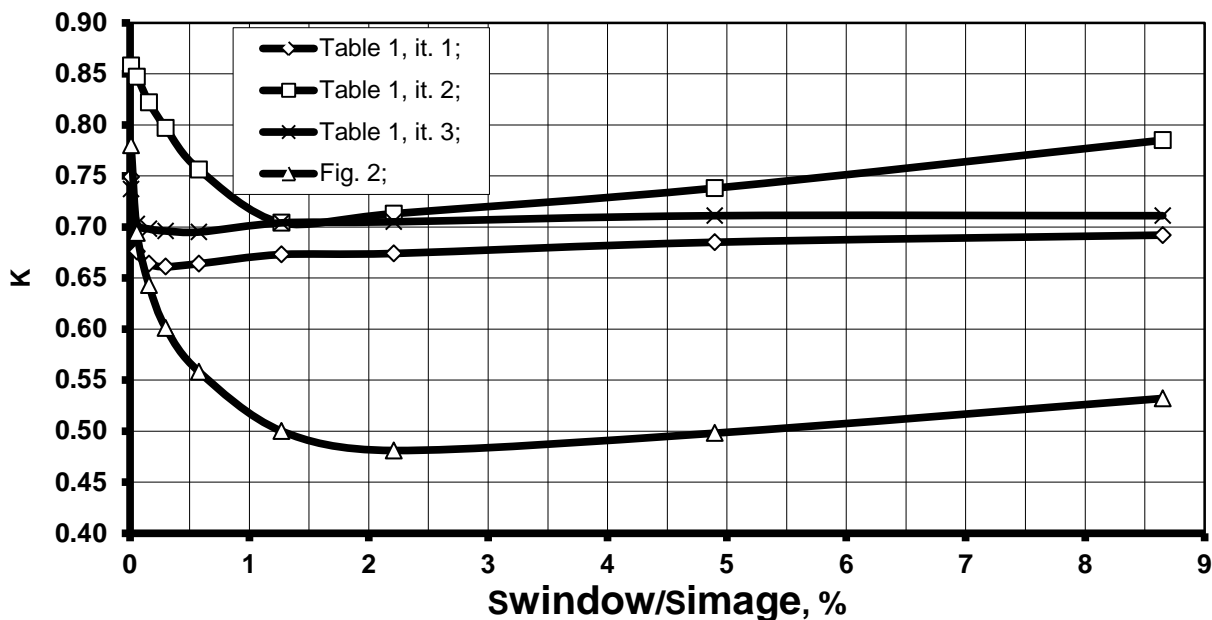
Figure 10: The impact of sliding window size on segmentation quality factor of water-oil emulsions

5. CONCLUSION

There is improved irregular pyramids method for processing the images of dispersed formations and other micro objects. The method is based on the natural aggregation of

adjacent areas in the image from one pyramid level to another and can process noisy images of different sized objects with non-uniform brightness.

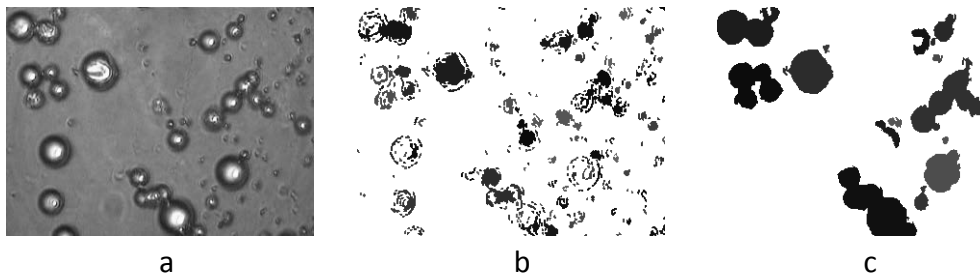Algorithms determining the neighboring areas in the image and internal hollows of connected set are designed on the basis of different types of pixels connectivity. Using proposed algorithms for constructing different hierarchical levels of Meer pyramid and dispersed formations images segmentation will provide more precise objects structure and avoid overdetalization. There is proposed method for sliding window size evaluation for local segmentation methods applied to processing dispersion environments images by irregular pyramids method. The software system is designed on the results of investigation.

REFERENCES

[1].   Gonzales, R.C. and Woods, R.E. (2005) Digital Image Processing, Tekhnosfera, Moscow, Russia.

[2].   Aulchenko, S. M., Latypov, A.F. and Nikulichev, Yu. V. (2000) "Curves and Surfaces Construction by Parametric polynomials", Avtometriya, no 4, pp. 60-75.

[3].   Honkanen, M. and Marjanen, K. (2007) Analysis of the overlapping images of irregularly-shaped particles, bubbles and droplets. Proc. of Int. Conf. on Multiphase Flow, Leibzig, Germany, paper 559.

[4].   Kutalik, Z., Razaz, M. and Baranyi J. (2004) "Occluding convex image segmentation for e.coli microscopy images" papers of the XII European Signal Processing Conference EUSIPCO, Viena, pp. 937–940.

[5].   Jun Zhang and Jinglu Hu (2008) "Image Segmentation Based on 2D Otsu Method with Histogram Analysis", International Conference on Computer Science and Software Engineering, Wuhan, Hubei, Vol. 6, pp. 105-108.

[6].   Ruzova, T., Yeliseyev, V., Tolstopyat, A. and Fleer, L. (2013) "Evaluating Geometrical Parameters of Disperse Structures by the Images", Signal Processing Research, Vol. 2, Issue: 2, pp. 49 – 54.

[7].   Meer P. (1989) "Stochastic image pyramids", Computer Vision Graphics Image Processing, 45:269–294.

[8].   Arhangelsky, A.Ya. (2000) Delphi 5 programming, ZAO "Izdatelstvo BINOM", Moscow, Russia.

ADVANCES IN
IMAGE AND VIDEO PROCESSING

On Supervised Methods for Segmentation of Blood Vessels in Ocular Fundus Images

Edward James, Antonio Francisco
School of Informatics and Computing, Indiana University Bloomington, USA;
Edward.james85@gmail.com, antonio.francisco01@gmail.com

ABSTRACT

Information about the retinal blood vessel network is important for diagnosis, treatment, screening, evaluation and the clinical study of many diseases such as diabetes, hypertension and arteriosclerosis. Automated segmentation and identification of retinal image structures had become one of the major research subjects in the fundus imaging and diagnostic ophthalmology. Automatic segmentation of blood vessels from retinal images is considered as first step in development of automated system for ophthalmic diagnosis. With the development of computational efficiency, the pattern classification and image processing techniques are increasingly used in all fields of medical sciences particularly in ophthalmology. In this paper, we have presented a review of supervised classification algorithms for retinal vessel segmentation available in the literature. We outline the principles upon which retinal vessel segmentation algorithms are based. We discuss current supervised classification techniques used to automatically detect the blood vessels.

Keywords: Image segmentation, Pattern Recognition, Supervised classification, Ocular Fundus, Retinal image analysis.

1. INTRODUCTIN

The eye is a unique region of the human body where the vascular condition can be directly observed in-vivo. By using an ophthalmoscope to look through the pupil, a magnified image of the retina and blood vessels can be observed that course across its anterior surface [1]. The blood vessels appear as elongated features in retinal images that are of different intensity than the background, and their thickness is always smaller than a certain value. They enter into the retina by the optic disc and form branches of vessels that are connected.

Information about the retinal vascular network is important for diagnosis, treatment, screening, evaluation and the clinical study of many diseases such as diabetes, hypertension

and arteriosclerosis [2]. Several eye diseases such as retinal artery occlusion and chorodial neovascularization [3] induce changes in the retinal vascular network [4]. Blood vessels are the most predominant and stable structures appearing in the ocular fundus, therefore reliable vessel extraction is a prerequisite for subsequent retinal image analysis and processing. Some of the main clinical objectives reported in the literature for retinal vessel segmentation are the implementation of screening programs for diabetic retinopathy [4, 5] evaluation of retinopathy of prematurity [6], foveal avascular region detection [7], arteriolar narrowing [8, 9], the relationship between vessel tortuosity and hypertensive retinopathy [10], vessel diameter measurement to diagnose cardiovascular diseases and hypertension [11, 12], and computer-assisted laser surgery [2, 13]. Other indirect applications include automatic generation of retinal maps for the treatment of age-related macular degeneration [14]; extraction of characteristic points of the retinal vasculature for temporal or multimodal image registration [15, 16]; retinal image mosaic synthesis [17]; identification of the optic disc position [18, 19], and localization of the fovea [20]; change detection [6, 21-23] and tracking in video sequences [24, 25]. All these techniques depend on vessel extraction. The network of retinal vessels is distinctive enough to each individual and can be used for biometric identification, although it has not yet been extensively explored [26]. Furthermore, the segmentation of the vascular tree seems to be the most appropriate representation for the image registration applications due to three of the following reasons: 1) it maps the whole retina; 2) it does not move except in a few diseases; 3) it contains enough information for the localization of some anchor points. Mostly vascular branching and crossover points are used as landmark features [27].

The quantification of vessel features, such as length, width and branching pattern, among others, can provide new insights to diagnose and stage pathologies which affect the morphological and functional characteristics of blood vessels. However, when the vascular network is complex, or the number of images is large, manual measurements can become tiresome or even impossible. A feasible solution is the use of automated analysis, which is nowadays commonly accepted by the medical community.
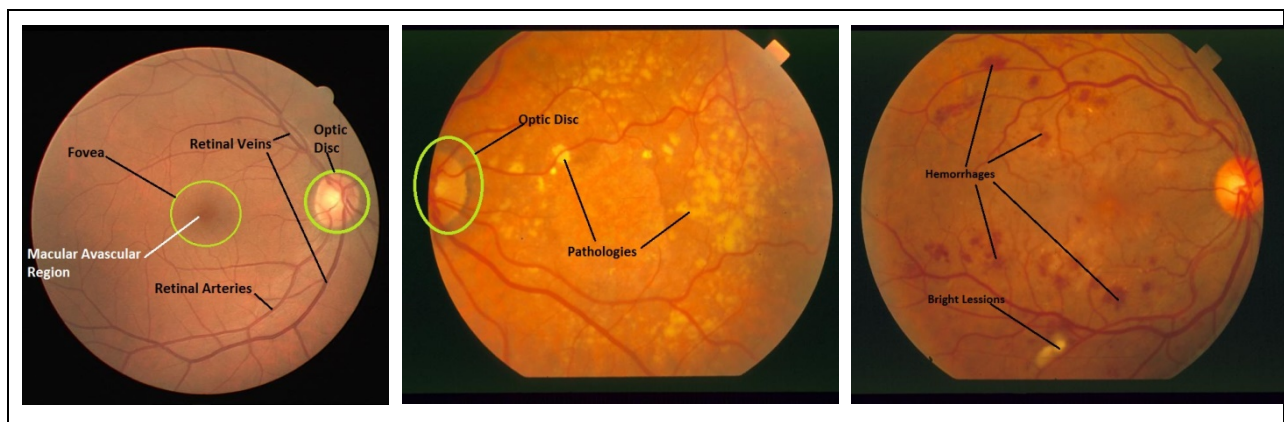

Figure 1: Anatomical Structures in Retinal Images

2. RETINAL BLOOD VESSELS MORPHOLOGY

The retinal vasculature is composed of arteries and veins, with their tributaries visible within the retinal image. There is a wide range of vessel widths ranging from one pixel to 17 pixels, depending on both the width of the vessel and the image resolution. The vessels have a lower reflectance compared to other retinal surfaces, thus, they usually appear darker relative to the background. The central intensity of some vessels differs from the background by as little as four grey levels, and the background noise standard deviation is almost 2.3 grey levels [28]. A variety of structures appear in the images, including the retina boundary, the optic disc, and pathologies. The pathologies are particularly challenging to automatic vessel extraction because they may appear as a series of bright spots, sometimes with narrow, darker gaps in between. Light is absorbed and reflected by the retinal vessels, the retinal capillaries and the choroid. Variations in the thickness of the vessel wall and the index of refraction have negligible influence on the apparent width of the blood column. However, occasionally a light streak running the length of the vessel is reflected from the transparent convex wall of the arteriole [12]. Retinal vessels also exhibit a strong reflection along their centerline known as central vessel reflex, which is more pronounced in arteries than veins, and is stronger at longer wavelengths. This effect is believed to result from a specular reflection at the interface between the retina and vitreous, the internal limiting membrane. Light reflexes and artifactual features such as specular reflection are typically found in the retinal images of younger patients. However, the thickening and fibrosis of the vessel wall associated with arteriosclerosis changes the refractive index and increases the width of the light reflex. The anatomical structures in retinal images are shown in Figure 1.

The vessel cross-sectional intensity profiles approximate a Gaussian shape, or a mixture of Gaussians in case of central vessel reflex. The orientation and grey level of a vessel does not change abruptly; they are locally linear and gradually change in intensity along their lengths. The vessels can be expected to be connected and, in the retina, form a binary treelike structure. However, the shape, size and local grey level of blood vessels can vary hugely and some background features may have similar attributes to vessels. Vessel crossing and branching can further complicate the profile model. As with the processing of most medical images, signal noise, drift in image intensity and lack of image contrast pose significant challenges to the extraction of blood vessels.

There are some reviews [29, 30] available in the literature which give an overview of vessel segmentation techniques from 2-D as well as 3-D images in various application domains including (i) extraction of neurovascular structures (ii) retinal blood vessel segmentation, (iii) coronary artery extraction, (iv) extraction of blood vessels from mammograms, (v) human airway tree (pulmonary tree) segmentation, (vi) extraction of abdominal aorta and vascular structures in the legs, (vii) extraction of vascular structures in livers, (viii) colon extraction, (ix) segmentation of nerve channels and (x) extraction of tubular structures for industrial and

scientific applications. Other studies [30-33] present an overview of different algorithms for feature extraction, segmentation and registration of retinal images. The surveys [5, 34] [38,39] on algorithms for automatic detection of diabetic retinopathy are also presented.

3. RETINAL BLOOD VESSEL SEGMENTATION

3.1   Materials

The retinal vessel segmentation methodologies are evaluated on the publically available databases for retinal images. The datasets are discussed below.

3.1.1   DRIVE Database

The DRIVE (Digital Retinal Images for Vessel Extraction)[35] is a publically available database, consisting of a total of 40 color fundus photographs. The photographs were obtained from a diabetic retinopathy screening program in the Netherlands. The screening population consisted of 453 subjects between 31 to 86 years of age. Each image has been JPEG compressed, which is common practice in screening programs. Of the 40 images in the database, 7 contain pathology, namely exudates, hemorrhages and pigment epithelium changes. The images were acquired using a Canon CR5 non-mydriatic 3CCD camera with a 45 degree field of view (FOV). Each image is captured using 8 bits per color plane at 768 × 584 pixels. The FOV of each image is circular with a diameter of approximately 540 pixels. The set of 40 images was divided into a test and training set both containing 20 images. Three observers, the first and second author and a computer science student manually segmented a number of images. All observers were trained by an experienced ophthalmologist (the last author). The first observer segmented 14 images of the training set while the second observer segmented the other 6 images. The test set was segmented twice resulting in a set X and Y. Set X was segmented by both the first and second observer (13 and 7 images respectively) while set Y was completely segmented by the third observer. The performance of the vessel segmentation algorithms is measured on the test set. In set X the observers marked 577,649 pixels as vessel and 3,960,494 as background (12.7% vessel). In set Y 556,532 pixels are marked as vessel and 3,981,611 as background (12.3% vessel). Figure 2 shows the retinal images from DRIVE database.

Figure 5: Retinal Images from DRIVE Database; (top row) Normal Image, (bottom row) Pathological Image. (a) Retinal image, (b) Segmented Vessels

3.1.2   STARE Database

The STARE database [36] contains 20 images for blood vessel segmentation; ten of these contain pathology. The digitized slides are captured by a TopCon TRV-50 fundus camera at 35° field of view (FOV). The slides were digitized to 605 x 700 pixels, 8 bits per colour channel. The approximate diameter of the FOV is 650x500 pixels. Two observers manually segmented all the images. The first observer segmented 10.4% of pixels as vessel, against 14.9% vessels for the second observer. The segmentations of the two observers are fairly different in that the second observer segmented many more of the thinner vessels than the first one. Performance is computed with the segmentations of the first observer as the ground truth. Figure 3 illustrates the retinal images form STARE database.
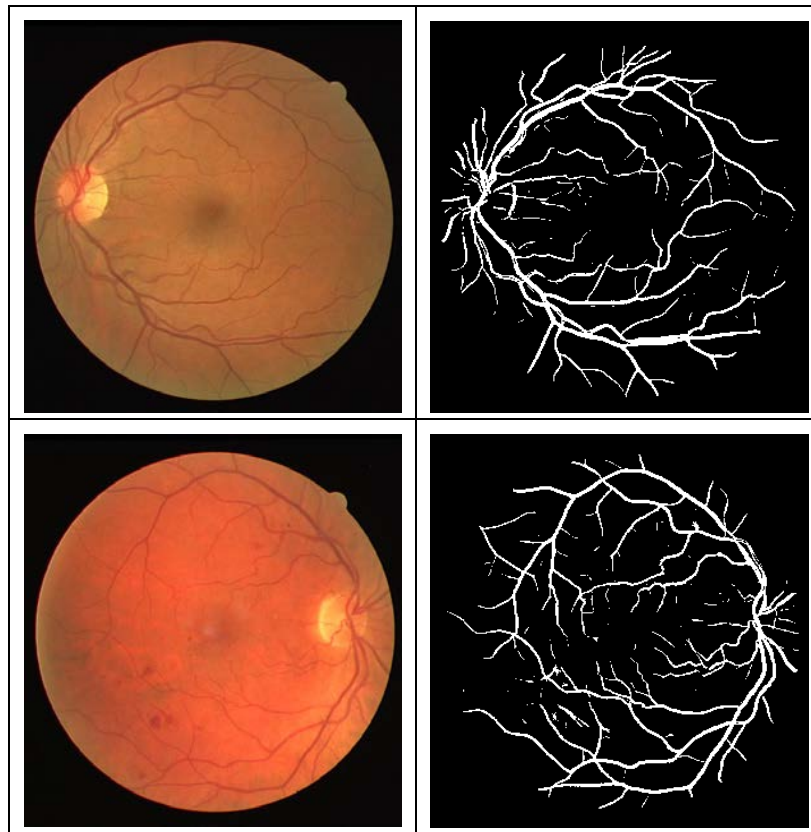
Figure 6: Retinal Images from STARE Database; (top row) Normal Image, (bottom row) Pathological Image. (a) Retinal image, (b) Segmented Vessels

3.2 Performance Measures

In the retinal vessel segmentation process, the outcome is a pixel-based classification result. Any pixel is classified either as vessel or surrounding tissue. Consequently, there are four events; two classifications and two misclassifications.

3.2.1 Classifications

The classifications are

- True Positive (TP) ; when a pixel is correctly segmented as a vessel pixel i.e. the pixel is classified as a vessel pixel and it is actually the vessel pixel as per the gold standard (the manual segmentation by an expert)

- True Negative (TN); when a pixel is correctly segmented as a non-vessel, the pixel is classified as a non-vessel pixel and it is actually the non-vessel pixel as per the gold standard.

3.2.2 Mis-Classifications

The two misclassifications are

- False Negative (FN) occurs when a pixel in a vessel is segmented in the non-vessel area, i.e. the pixel is classified as non-vessel but actually it belongs to a vessel as per the gold standard.

- False Positive (FP) occurs when a non-vessel pixel is segmented as a vessel-pixel i.e. the pixel is actually the non-vessel pixel (as per the gold standard) but is classified as the vessel pixel.

The measures derived from the above events are

3.2.3   True Positive Rate

True Positive Rate (TPR) or true positive fraction represents the fraction of pixels correctly detected as vessel pixels. It is the ratio between the numbers of pixels correctly detected as vessel pixels to the count of pixels which are actually in vessels.

$$TPR = \frac{\text{\# of pixels correctly detected as vessel pixel}}{\text{\# of pixels actually in vessels}}$$

3.2.4   False Positive Rate

False Positive Rate (FPR) or false positive fraction represents the fraction of pixels erroneously detected as vessel pixels. It is obtained as the ration between the numbers of pixels erroneously detected as vessel pixels to the number of pixels which are actually in non-vessel region in the retinal image.

$$FPR = \frac{\text{\# of pixels erroneously detected as vessel pixel}}{\text{\# of pixels actually in non-vessels region}}$$

3.2.5   Accuracy

The accuracy is estimated by the ratio of the total number of correctly classified pixels (sum of true positives and true negatives) by the number of pixels in the image FOV.

$$Accuracy = \frac{\text{\# of correctly classified pixels}}{\text{\# of pixels in image FOV}}$$

3.2.6   Sensitivity

Sensitivity (SN) reflects the ability to detect vessel pixels. The sensitivity of a vessel detection algorithm is a measure of how well the algorithm performs in correctly identifying vessel pixels within a retinal fundus image.

Sensitivity is expressed as

$$SN = \frac{TP}{(TP + FN)}$$

Where, TP and FN are the number of true positive and false negative results, respectively. Sensitivity can also be thought as 1- the False Negative Rate.

3.2.7 Specificity

Specificity (SP) is the ability to detect non-vessel pixels. The specificity of a vessel segmentation algorithm reflects how good the algorithm is correctly identifying the non-vessel pixels.

The formula for specificity is

$$SP = \frac{TN}{(TN + FP)}$$

Where, TN and FP are the number of true negative and false positive results, respectively. Specificity can also be written as,

$$SP = 1 - FPR$$

3.2.8 ROC Analysis

A receiver operating characteristic (ROC) curve plots the fraction of vessel pixels correctly classified as vessel, namely the true positive rate (TPR), versus the fraction of non-vessel pixels wrongly classified as vessel, namely the false positive rate (FPR). The closer the curve approaches the top left corner; the better is the performance of the system. The most frequently used performance measure extracted from the ROC curve is the value of the area under the curve (AUC) which is 1 for an optimal system. For retinal images, TPR and FPR are computed considering only pixels inside the FOV.

4. SUPERVISED METHODS FOR RETINAL VESSEL SEGMENTATION

Supervised methods exploit some prior labeling information to decide whether a pixel belongs to a vessel or not, while unsupervised methods perform the vessel segmentation without any prior labeling knowledge. In supervised methods, the rule for vessel extraction is "learned" by the algorithm on the basis of a training set of manually processed and segmented reference images often termed as "gold standard". This gold standard data set consists of a number of images whose vascular structure must be precisely marked by an ophthalmologist. However, as noted by Hoover et al. [37] there is significant disagreement in the identification of vessels even amongst expert observers. These methods classify individual pixels and require hand-labeled gold standard images for training. In a supervised method, the criteria are determined by the ground truth data based on given features. However, a prerequisite for a supervised method is the availability of the ground truth data that are already classified, which may not be available in real life applications. As supervised methods are designed based on pre-classified data, their performance is usually better than that of unsupervised ones and can produce very good results for healthy retinal images.

Artificial neural networks have been extensively investigated for segmenting retinal features such as the vasculature[38] making classifications based on statistical probabilities

rather than objective reasoning. These neural networks employ mathematical "weights" to decide the probability of input data belonging to a particular output. This weighting system can be adjusted by training the network with data of known output typically with a feedback mechanism to allow retraining.

Nekovei and Sun [39] describe an approach using a back-propagation network for the detection of blood vessels in X-ray angiography. The method applies the neural network directly to the angiogram pixels without prior feature detection. The pixels of the small sub-window which slides across the angiogram image, are directly fed as input to the network. The feature vectors are formed by gray-scale values from the sub window centered on the pixel being classified. The ground truth images of manually labeled angiograms are used as the training set to set the network's weights. A modified version of the common delta-rule is to obtain these weights. The proposed method does not extract the vascular structure but is to label the pixels as vessel or non-vessel.

Sinthanayothin et al. [40] preprocessed images with PCA to reduce background noise by reducing the dimensionality of the data set and then applied a neural network to identify the pathology. They reported a success rate of 99.56% for the training data and 96.88% for the validation data, respectively, with an overall sensitivity and specificity of 83.3% (standard deviation 16.8%) and 91% (standard deviation 5.2%), respectively. The result of the approach was compared with an experienced ophthalmologist manually mapping out the location of the blood vessels in a random sample of seventy three 20×20 pixel windows and requiring an exact match between pixels in both images.

Niemeijer et al. [41] extracts a feature vector for each pixel that consists of the Gaussian and its derivatives up to order 2 at scales s = 1, 2, 4, 8, 16 pixels, augmented with the green plane of the RGB image and then, uses a k-nearest neighbor (kNN) algorithm to estimate the probability of the pixel belonging to a vessel. Each feature is normalized to zero mean and unit variance before classification. By thresholding the probability map a binary segmentation of the vasculature can be obtained. The algorithm is tested on the DRIVE data set resulting in average accuracy of 0.9416 and area under the ROC curve of 0.9294

Staal et al. [42] presented a ridge based vessel segmentation methodology from colored images of the retina which exploits the intrinsic property that vessels are elongated structures. The technique is based on an extraction of image ridges, which are natural indicators of vessels and coincide approximately with vessel centerlines. Image primitives are computed by grouping the ridge pixels, therefore grouping the ridges to sets that approximate straight line elements. With these sets an image is partitioned into patches by assigning each image pixel to the closest line element. Every line element constitutes a local coordinate frame for its corresponding patch. Every line element defines a local coordinate frame termed as an affine convex set region within each patch, in which local features are extracted for every pixel. In total, 27 features are selected from convex set regions collectively as well as from individual pixels using

a sequential forward selection method. A K-NN classifier is used for classification. Some authors suggests [43] that by combining ridge features across multiple scales, the local vessel size is decoupled from the model. The methodology is tested on the publically available STARE [37] and Utrecht database obtained from a screening programme in the Netherlands. The method achieves an average accuracy of 0.9516 and an area under the ROC curve of 0.9614 on the STARE dataset.

The use of a 2-D gabor wavelet and supervised classification for retinal vessel segmentation has been demonstrated by Soares et al. [44]. Each pixel is represented by a feature vector composed of the pixel's intensity and two-dimensional Gabor wavelet transform responses taken at multiple scales. A Gaussian mixture model (a Bayesian classifier in which each class-conditional probability density function is described as a linear combination of Gaussian functions) classifier is used to classify each pixel as either a vessel or non-vessel pixel. The probability distributions are estimated based on a training set of labeled pixels obtained from manual segmentations. The methodology is evaluated on the DRIVE and STARE datasets resulting in average accuracy of 0.9466 & 0.9480 and the area under the ROC curve as 0.9614 & 0.9671 for DRIVE and STARE respectively. The algorithm takes in to account the information local to each pixel through image filters, ignoring useful information from shapes and structures present in the image. It does not work very well on the images with non-uniform illumination as it produces false detection in some images on the border of the optic disc, hemorrhages and other types of pathologies that present strong contrast.

Ricci et al. [45] proposed a methodology to segment retinal vessels using line operators and support vector classification. A line detector which is based on the evaluation of the average grey level along lines of fixed length passing through the target pixel at different orientations is applied to the green channel of an RGB image and the response is thresholded to obtain unsupervised pixel classification. Moreover, two orthogonal line detectors are also employed along with the grey level of the target pixel to construct a feature vector for supervised classification using a support vector machine. With respect to other supervised techniques, the algorithm 1) requires fewer features, 2) feature extraction is computationally simpler, and 3) fewer examples are needed for training. The algorithm makes use of local differential computation of the line strength which makes the line detector robust with respect to non-uniform illumination and contrast. Also the line detector behavior in the presence of a central reflex is quite satisfactory. The performance of both methods is evaluated on the publicly available DRIVE and STARE databases through ROC analysis, resulting in average accuracy of 0.9563 & 0.9584 and the area under ROC curve as 0.9558 & 0.9602 for DRIVE and STARE respectively.

Osareh and Shadgar [46] use multiscale Gabor filters for vessel candidate identification, then the features are extracted using principal component analysis. The parameters for Gabor filters are optimally tuned with experimentations. The image pixels are classified as vessels and

non-vessels using the corresponding feature vectors by Gaussian mixture model (GMM) and support vector machines (SVM). The methodology is tested on DRIVE as well as on the author's dataset consisting of 90 normal and abnormal images. The classification accuracy obtained is 95.24%, with 96.14% sensitivity and 94.84% specificity with GMM. The best overall accuracy, using optimal parameters for SVM is 96.75% with 96.50% sensitivity and 97.10% specificity. The methodology achieves area under the ROC curve as 0.965 on the DRIVE database. However, there are some false positives due to background noise and non-uniform illumination, the border of the optic disc and other types of pathologies and the thinnest vessels are also not detectable, however, these thin vessels are not of much clinical importance.

Salem et al [47] proposed a RAdius based Clustering ALgorithm (RACAL) which uses a distance based principle to map the distributions of the image pixels. A partial supervision strategy is combined with the clustering algorithm. The features used are the green channel intensity, the local maxima of the gradient magnitude, and the local maxima of the large eigenvalue calculated from Hessian matrix. The same features are used with kNN and RACAL algorithms and later perform better for the detection of small vessels. The methodology attains a specificity of 0.9750 and sensitivity of 0.8215 on the STARE database.

Xu and Luo [48] combines several image processing techniques with support vector machine(SVM) classification for vessel segmentation. In this methodology, the background of the green channel is normalized, the large vessels are segmented using adaptive local thresholding and the optic disk edges are removed. The original image is then processed by wavelets at multiple scales for feature extraction. The line detectors are used to identify thin vessels. A 12 dimensional feature vector for each residual pixel in the binary retinal image excluding large vessels is constructed and a support vector machine is used to distinguish thin vessel segments from all the fragments. A tracking method based on a combination of vessel direction and the eigenvector of the Hessian matrix is used for thin vessel growth to obtain a segmented vessel tree. The method achieves an average accuracy of 0.9328 and an average sensitivity of 0.7760 on the DRIVE database.

Lupascu et al. [49] introduces another supervised method known as feature-based AdaBoost classifier (FABC) for vessel segmentation. The 41-D feature vector is a rich collection of measurements at different spatial scales ($\sqrt2$, 2, $2\sqrt2$ and 4), including the output of various filters (Gaussian and derivatives of Gaussian filters, matched filters, and 2-D Gabor wavelet transform), and the likelihood of structures like edges and ridges via numerical estimation of the differential properties of the intensity surface (principal and mean curvatures, principal directions, and root mean square gradient). This feature vector encodes a rich description of vessel-related image properties, namely local (pixel's intensity and Hessian-based measures), spatial (e.g., the gray-level profile of the cross section of a vessel can be approximated by a Gaussian curve) and structural (e.g., vessels are geometrical structures, which can be seen as tubular). An AdaBoost classifier is trained on 789,914 gold standard examples of vessel and

non-vessel pixels. The method achieves an average accuracy of 0.9597, an area under the ROC curve of 0.9561 and a kaapa measure of 0.72 on the DRIVE dataset. The strength of FABC lies in its capturing a rich collection of shape and structural information, in addition to local information at multiple spatial scales, in the feature vector. FABC does not discuss the issues related to the connection of broken vessel segments and some local ambiguities present due to the convergence of multiple and variously bent vessels.

The combination of the radial projection and the semi-supervised self-training method using SVM is employed by X. You [50] for vessel segmentation. The vessel centerlines and the narrow and low contrast blood vessels are located using radial projections. A modified steerable complex wavelet is employed for vessel enhancement. The line strength measures are applied to the vessel enhanced image to generate the feature vector. The SVM classifier is used in a semi-supervised self-training to extract the major structure of vessels. The segmented vasculature is obtained by the union of the two. The algorithm self learns from human-labeled data and weakly labeled data therefore yielding good results with decrease in the detection of false vessels. The method is very good in detecting narrow and low contrast vessels but prone to errors in case of pathologies. The average accuracy, sensitivity and specificity on the DRIVE database is 0.9434, 0.7410, and 0.9751 respectively and for the STARE database 0.9497, 0.7260, and 0.9756 respectively.

Marin [51] presented a neural network based supervised methodology for the segmentation of retinal vessels. The methodology uses a 7-D feature vector composed of gray-level and moment invariant-based features. A multilayer feed forward neural network is utilized for training and classification. The input layer consists of seven neurons, the three hidden layers consist of fifteen neurons each and output layer is comprised of single neuron. The method proves to be effective and robust with different image conditions and on multiple image databases even if the neural network is trained on only one database. The average accuracy, AUC, sensitivity and specificity on the DRIVE database is 0.9452, 0.9588, 0.7067, and 0.9801 respectively and for the STARE database 0.9526, 0.9769, 0.6944, and 0.9819 respectively.

Fraz et. al. [52] presented an effective retinal vessel segmentation technique based on supervised classification using an ensemble classifier of boosted and bagged decision trees. Their methodology has used a nine dimensional feature vector which consists of the vessel map obtained from the orientation analysis of the gradient vector field, the morphological transformation; line strength measures and the Gabor filter response which encodes information to successfully handle both normal and pathological retinal images. The important feature of bagged ensemble is that the reliable estimates of the classification accuracy and feature importance are obtained during the training process without supplying the test data. The ensemble classifier was constructed by using 200 weak learners and is trained on 200,000 training samples randomly extracted from the training set of the DRIVE and 75000 samples from STARE databases. These parameters are chosen by empirically analyzing the out-of-bag

classification for a given number of training samples and the decision trees. The average accuracy, AUC, sensitivity and specificity on the DRIVE database is 0.9480, 0.9747, 0.7406, and 0.9807 respectively and for the STARE database 0.9534, 0.9768, 0.7548, and 0.9763 respectively.

Table 1: Summary of supervised classification algorithms for vessel segmentation

Methodology	Database	Sensitivity	Specificity	Accuracy	Area under ROC
Human Observer	DRIVE	0.797	0.972	0.9473	-
	STARE	-	-	0.9354	-
Sinthanayothin	Local Dataset	0.833	0.91	-	-
Niemeijer	DRIVE	-	-	0.9416	0.9294
Staal	DRIVE	-	-	0.9442	0.952
	STARE	-	-	0.9516	0.9614
Soares	DRIVE	-	-	0.9466	0.9614
	SATRE	-	-	0.9480	0.9671
Ricci	DRIVE	-	-	0.9563	0.9558
	STARE	-	-	0.9584	0.9602
Osareh and Shadgar	DRIVE (SVM)	0.9650	0.9710	0.9675	0.974
	DRIVE(GMM)	0.9614	0.9484	0.9524	0.965
Salim	STARE	0.8215	0.9750	-	-
Lupascu	DRIVE	-	-	0.9597	0.9561
Xu and Luo	DRIVE	0.7760	-	0.9328(0.0075)	-
You et al., 2011 [50]	DRIVE	0.7410	0.9751	0.9434	
	STARE	0.7260	0.9756	0.9497	
Marin et al., 2011 [51]	DRIVE	0.7067	0.9801	0.9452	0.9588
	STARE	0.6944	0.9819	0.9526	0.9769
Fraz et al. [52]	DRIVE	0.7406	0.9807	0.9480	0.9747
	STARE	0.7548	0.9763	0.9534	0.9768

5. CONCLUSION

Retinal digital image analysis is able to exploit the ease with which the retinal circulation can be visualized, photographed, and analyzed non-invasively in vivo. Using objective, quantitative measures from retinal vasculature which are based on principals of optimization of a branching vasculature, studies have been able to improve our understanding of the effect of systemic factors on the microvasculature. The most commonly performed quantitative measurement from digital retinal vascular image analysis has

been the AVR. Whilst this has proved to be a very useful research tool to measure generalized arteriolar narrowing, very large epidemiological studies have been required to have sufficient statistical power to be able to detect associations of this entity with systemic factors. It is also unclear from current studies whether the detection of retinal microvascular changes has additional predictive value above current standardized methods. With an increasingly aged population and increased strain on medical resources, the use of strategies such as telemedicine and widespread screening of individuals at risk of certain diseases will increase. Retinal vascular digital image analysis will play an ever greater role in clinical ophthalmology.

REFERENCES

[1]. Abràmoff, M.D., M.K. Garvin, and M. Sonka, *Retinal Imaging and Image Analysis.* Biomedical Engineering, IEEE Reviews in, 2010. **3**: p. 169-208.

[2]. Kanski, J.J., *Clinical ophthalmology*. 6th edition ed2007, London: Elsevier Health Sciences (United Kingdom). 952.

[3]. Liang, Z., et al., *The detection and quantification of retinopathy using digital angiograms.* Medical Imaging, IEEE Transactions on, 1994. **13**(4): p. 619-626.

[4]. Teng, T., M. Lefley, and D. Claremont, *Progress towards automated diabetic ocular screening: A review of image analysis and intelligent systems for diabetic retinopathy.* Medical and Biological Engineering and Computing, 2002. **40**(1): p. 2-13.

[5]. Winder, R.J., et al., *Algorithms for digital image processing in diabetic retinopathy.* Computerized Medical Imaging and Graphics, 2009. **33**(8): p. 608-622.

[6]. Heneghan, C., et al., *Characterization of changes in blood vessel width and tortuosity in retinopathy of prematurity using image analysis.* Medical image analysis, 2002. **6**(4): p. 407-429.

[7]. Haddouche, A., et al., *Detection of the foveal avascular zone on retinal angiograms using Markov random fields.* Digital Signal Processing. **20**(1): p. 149-154.

[8]. Narasimha-Iyer, H., et al., *Automatic Identification of Retinal Arteries and Veins From Dual-Wavelength Images Using Structural and Functional Features.* Biomedical Engineering, IEEE Transactions on, 2007. **54**(8): p. 1427-1435.

[9]. Hatanaka, Y., et al. *Automated analysis of the distributions and geometries of blood vessels on retinal fundus images*. SPIE.

[10]. Foracchia, M., *Extraction and quantitative description of vessel features in hypertensive retinopathy fundus images*, in *Book Abstracts 2nd Int. Workshop on Computer Assisted Fundus Image Analysis*, E. Grisan, Editor 2001. p. 6-6.

[11]. Xiaohong, G., et al. *A method of vessel tracking for vessel diameter measurement on retinal images*. in *Image Processing, 2001. Proceedings. 2001 International Conference on*.

[12]. Lowell, J., et al., *Measurement of retinal vessel widths from fundus images based on 2-D modeling.* Medical Imaging, IEEE Transactions on, 2004. **23**(10): p. 1196-1204.

[13]. Hong, S., et al., *Optimal scheduling of tracing computations for real-time vascular landmark extraction from retinal fundus images.* Information Technology in Biomedicine, IEEE Transactions on, 2001. **5**(1): p. 77-91.

[14]. Pinz, A., et al., *Mapping the human retina.* Medical Imaging, IEEE Transactions on, 1998. **17**(4): p. 606-619.

[15]. Zana, F. and J.C. Klein, *A multimodal registration algorithm of eye fundus images using vessels detection and Hough transform.* Medical Imaging, IEEE Transactions on, 1999. **18**(5): p. 419-428.

[16]. Can, A., et al., *A Feature-Based, Robust, Hierarchical Algorithm for Registering Pairs of Images of the Curved Human Retina.* IEEE Transactions on Pattern Analysis and Machine Intelligence, 2002. **24**: p. 347-364.

[17]. Fritzsche, K., et al., *Automated Model Based Segmentation, Tracing and Analysis of Retinal Vasculature from Digital Fundus Images*, in *State-of-The-Art Angiography, Applications and Plaque Imaging Using MR, CT, Ultrasound and X-rays*2003, Academic Press. p. 225-298.

[18]. Hoover, A. and M. Goldbaum, *Locating the optic nerve in a retinal image using the fuzzy convergence of the blood vessels.* Medical Imaging, IEEE Transactions on, 2003. **22**(8): p. 951-958.

[19]. Foracchia, M., E. Grisan, and A. Ruggeri, *Detection of optic disc in retinal images by means of a geometrical model of vessel structure.* Medical Imaging, IEEE Transactions on, 2004. **23**(10): p. 1189-1195.

[20]. Huiqi, L. and O. Chutatape, *Automated feature extraction in color retinal images by a model based approach.* Biomedical Engineering, IEEE Transactions on, 2004. **51**(2): p. 246-254.

[21]. Fritzsche, K.H., *Computer vision algorithms for retinal vessel detection and width change detection*, 2004, Rensselaer Polytechnic Institute: Troy, NY, USA.

[22]. Houben, A.J.H.M., et al., *Quantitative analysis of retinal vascular changes in essential and renovascular hypertension.* Journal of hypertension, 1995. **13**(12).

[23]. Wasan, B., et al., *Vascular network changes in the retina with age and hypertension.* Journal of hypertension, 1995. **13**(12).

[24]. Koozekanani, D., et al., *Tracking the Optic Nerve Head in OCT Video Using Dual Eigenspaces and an Adaptive Vascular Distribution Model.* Computer Vision and Pattern Recognition, IEEE Computer Society Conference on, 2001. **1**: p. 934.

[25]. Solouma, N.H., et al., *A new real-time retinal tracking system for image-guided laser treatment.* Biomedical Engineering, IEEE Transactions on, 2002. **49**(9): p. 1059-1067.

[26]. Mari, et al., *Personal authentication using digital retinal images.* Pattern Anal.Appl., 2006. **9**(1): p. 21-33.

[27]. Chia-ling, T., et al., *Model-based method for improving the accuracy and repeatability of estimating vascular bifurcations and crossovers from retinal fundus images*, 2004.

[28]. Sofka, M. and C.V. Stewart, *Retinal Vessel Centerline Extraction Using Multiscale Matched Filters, Confidence and Edge Measures.* Medical Imaging, IEEE Transactions on, 2006. **25**(12): p. 1531-1546.

[29]. Kirbas, C. and F. Quek, *A review of vessel extraction techniques and algorithms.* ACM Comput.Surv., 2004. **36**(2): p. 81-121.

[30]. Fraz, M.M., et al., *Blood vessel segmentation methodologies in retinal images – A survey.* Computer methods and programs in biomedicine, 2012. **108**(1): p. 407-433.

[31]. Mabrouk, M.S., N.H. Solouma, and Y.M. Kadah, *Survey of Retinal Image Segmentation and Registration.* ICGST International Journal on Graphics, Vision and Image Processing, 2006. **6**(2): p. 1-11}.

[32]. Patton, N., et al., *Retinal image analysis: Concepts, applications and potential.* Progress in retinal and eye research, 2006. **25**(1): p. 99-127.

[33]. Stewart, C., et al., *Computer Vision Algorithms for Retinal Image Analysis: Current Results and Future Directions*, in *Computer Vision for Biomedical Image Applications*2005, Springer Berlin / Heidelberg. p. 31-50.

[34]. Faust, O., et al., *Algorithms for the Automated Detection of Diabetic Retinopathy Using Digital Fundus Images: A Review.* Journal of medical systems: p. 1-13.

[35]. Niemeijer, M., et al., *DRIVE: Digital Retinal Images for Vessel Extraction*, 2004.

[36]. *STARE: STructured Analysis of the Retina, http://www.ces.clemson.edu/~ahoover/stare/.* 2000.

[37]. Hoover, A.D., V. Kouznetsova, and M. Goldbaum, *Locating blood vessels in retinal images by piecewise threshold probing of a matched filter response.* Medical Imaging, IEEE Transactions on, 2000. **19**(3): p. 203-210.

[38]. Akita, K. and H. Kuga, *A computer method of understanding ocular fundus images.* Pattern Recognition, 1982. **15**(6): p. 431-443.

[39]. Nekovei, R. and S. Ying, *Back-propagation network and its configuration for blood vessel detection in angiograms.* Neural Networks, IEEE Transactions on, 1995. **6**(1): p. 64-72.

[40]. Sinthanayothin, C., et al., *Automated localisation of the optic disc, fovea, and retinal blood vessels from digital colour fundus images.* British Journal of Ophthalmology, 1999. **83**(8): p. 902-910.

[41]. Abramoff, M.N., et al. *Comparative study of retinal vessel segmentation methods on a new publicly available database*. in *SPIE Medical Imaging*. 2004. SPIE.

[42]. Staal, J., et al., *Ridge-based vessel segmentation in color images of the retina.* Medical Imaging, IEEE Transactions on, 2004. **23**(4): p. 501-509.

[43]. Li, W., A. Bhalerao, and R. Wilson, *Analysis of Retinal Vasculature Using a Multiresolution Hermite Model.* Medical Imaging, IEEE Transactions on, 2007. **26**(2): p. 137-152.

[44]. Soares, J.V.B., et al., *Retinal vessel segmentation using the 2-D Gabor wavelet and supervised classification.* Medical Imaging, IEEE Transactions on, 2006. **25**(9): p. 1214-1222.

[45]. Ricci, E. and R. Perfetti, *Retinal Blood Vessel Segmentation Using Line Operators and Support Vector Classification.* Medical Imaging, IEEE Transactions on, 2007. **26**(10): p. 1357-1365.

[46]. Osareh, A. and B. Shadgar, *Automatic Blood Vessel Segmentation In Color Images Of Retina.* Iranian Journal Of Science And Technology Transaction B-Engineering, 2009. **33**(B2): p. 191-206.

[47]. Salem, S., N. Salem, and A. Nandi, *Segmentation of retinal blood vessels using a novel clustering algorithm (RACAL) with a partial supervision strategy.* Medical and Biological Engineering and Computing, 2007. **45**(3): p. 261-273.

[48]. Xu, L. and S. Luo, *A novel method for blood vessel detection from retinal images.* BioMedical Engineering OnLine, 2010. **9**(1): p. 14.

[49]. Lupascu, C., et al., *A Comparative Study on Feature Selection for Retinal Vessel Segmentation Using FABC*, in *Computer Analysis of Images and Patterns*2009, Springer Berlin / Heidelberg. p. 655-662.

[50]. You, X., et al., Segmentation of retinal blood vessels using the radial projection and semi-supervised approach. Pattern Recognition, Volume 44, Issues 10–11, Pages 2314–2324

[51]. Marin, D., et al., *A New Supervised Method for Blood Vessel Segmentation in Retinal Images by Using Gray-Level and Moment Invariants-Based Features.* Medical Imaging, IEEE Transactions on, 2011. **30**(1): p. 146-158.

[52]. Fraz, M.M., et al., *An Ensemble Classification-Based Approach Applied to Retinal Blood Vessel Segmentation.* Biomedical Engineering, IEEE Transactions on, 2012. **59**(9): p. 2538-2548.